To appear in: IEEE ICRA 2012 International Conference on Robotics and Automation, Saint Paul, Minnesota, USA, May 2012

A MRI-Guided Concentric Tube Continuum Robot with Piezoelectric Actuation: A Feasibility Study

Hao Su†, Diana C. Cardona†, Weijian Shang, Alexander Camilo, Gregory A. Cole, D. Caleb Rucker, Robert J. Webster, III and Gregory S. Fischer

***Abstract*— This paper presents a versatile magnetic resonance imaging (MRI) compatible concentric tube continuum robotic system. The system enables MR image-guided placement of a curved, steerable active cannula. It is suitable for a variety of clinical applications including image-guided neurosurgery and percutaneous interventions, along with procedures that involve accessing a desired image target, through a curved trajectory. This 6 degree-of-freedom (DOF) robotic device is piezoelectrically actuated to provide precision motion with joint-level precision of better than 0.03mm, and is fully MRI-compatible allowing simultaneous robotic motion and imaging with no image quality degradation. The MRI compatibility of the robot has been evaluated under 3 Tesla MRI using standard prostate imaging sequences, with an average signal to noise ratio loss of less than 2% during actuator motion. The accuracy of active cannula control was evaluated in benchtop trials using an external optical tracking system with RMS error in tip placement of 1.00mm. Preliminary phantom trials of three active cannula placements in the MRI scanner showed cannula trajectories that agree with our kinematic model, with a RMS tip placement error of 0.61 - 2.24 mm.**

Keywords: MRI-compatible robot, Image-guided needle placement, Concentric tube continuum robot, Active cannula, Percutaneous interventions, Stereotactic surgery.

I. INTRODUCTION

IMAGE-GUIDED surgery (IGS) enables interventional procedures with greater precision and superior outcomes due to integration of medical imaging with the surgical workflow. However, traditional IGS typically relies on previously acquired images, while intra-operative imaging enables "closed-loop medicine" by providing a feedback pathway. MRI is an ideal guidance modality with the ability to perform high quality, volumetric, real-time, multi-parametric imaging with high soft tissue contrast without ionizing radiation.

Robot-assisted minimally invasive surgery offers significant advantages over manual approaches in applications requiring high accuracy and high reliability. Recently, considerable efforts have also been expended for needle based percutaneous interventions utilizing different imaging modalities, including ultrasound [1], computed tomography [2], and MRI [3] [4] [5]. A steerable needle not only enables focal therapy that enhances intervention efficacy by compensating for sources of error during insertion, but also reduces invasiveness by minimizing the number of repeated needle insertions required. In particular, there are a number of different approaches to steer flexible needles, including needle base manipulation of symmetric-tip needles [6] [7], bevel tip needle steering [8] and use of multiple concentric tubes [9] [10], among other methods. In this paper we focus on the concentric tube design, due to its ability to "steer" through open spaces as well as soft tissues. These robots change shape as individual tubes in the concentric collection are telescopically extended and axially rotated with respect to one another. It can be used as a miniature manipulator with a gripper [11], and has also been used without a gripper in soft tissues as a steerable needle [12] [13], which is our primary interest in this paper.

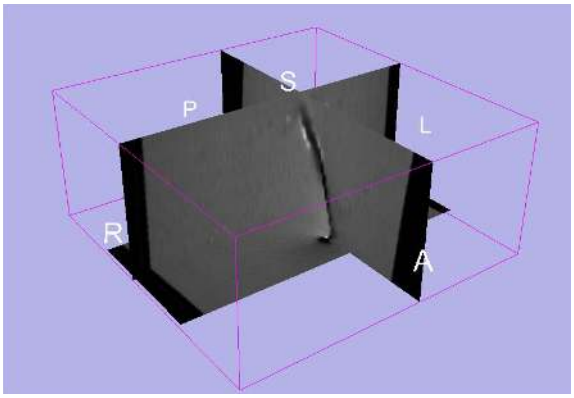

Fig. 1. Volumetric MRI showing a representative active cannula path inserted into a phantom by the robot inside the MRI scanner. The cannula is inserted along the I-S direction (vertical in this figure) and is shown in the sagittal plane along with additional two cross-sectional planes.

Deploying concentric tube active cannula inside MRI synergizes the visual capability of MRI with the dexterity and manipulability of robotic surgical assistance. Intra-operative MRI-guided surgery has been performed in several pioneering hospitals with improved surgical outcomes, including neurosurgery [14] and pneumatic robot-assisted prostate biopsy [15]. From the actuation perspective, Stoianovici et al. have developed MRI-compatible pneumatic stepper motors and applied them to brachytherapy seed placement [5]. Yang et al. [16] also investigated pneumatic motor for breast cancer biopsy diagnosis. Two generations of pneumatic needle placement systems [3], [17], [18] have also been developed. Piezoelectric actuation has been utilized for open MRI [19] and for operating in closed-bore MRI [20]. However, imaging noise during combined imaging and motion is evident with commercially available piezoelectric drivers [21] [22].

In our previous research efforts we have independently developed custom piezoelectric actuator drivers allowing

H. Su, W. Shang, A. Camilo, G.A. Cole and G.S. Fischer are with Automation and Interventional Medicine (AIM) Robotics Laboratory, Department of Mechanical Engineering, Worcester Polytechnic Institute, 100 Institute Road, Worcester, MA 01609, USA [haosu, gfischer]@wpi.edu

D. Cardona, D. C. Rucker and R. J. Webster III are with Vanderbilt University, Nashville, TN 37235, USA [diana.c.cardona, robert.webster]@vanderbilt.edu

†Shared first authorship.

simultaneous imaging with robot motion, and approaches for modeling and control of active cannulas. The primary contribution of this paper is the development of a system for manipulating active cannulas under MR image guidance - we demonstrate feasibility on in benchtop experiments and perform phantom trials in 3T MRI. A representative controlled curved trajectory is shown in the MRI volume in Fig. 1.

II. SYSTEM CONCEPT AND ARCHITECTURE

We adapt the needle placement robot described in [23] [24] such that the robot supports control of three concentric tubes. The robot is MRI-compatible and resides inside the MRI scanner bore during a procedure. The MRI robot controller, adapted from [25], resides inside the MRI scanner room beside the scanner bed.

The system is controlled from a workstation outside the scanner room connected via a fiber optic communication link to the robot controller. On the workstation is the modular robot control software shown in Fig. 2 that can be used to directly control the robot or interface with a navigation system such as 3D Slicer over OpenIGTLink [26]. This software incorporates registration between the robot and MR image space such that a specific location in the MR image volume can be targeted. Inside this platform, we can incorporate the forward and inverse kinematics for the robot, which are described in Section III.

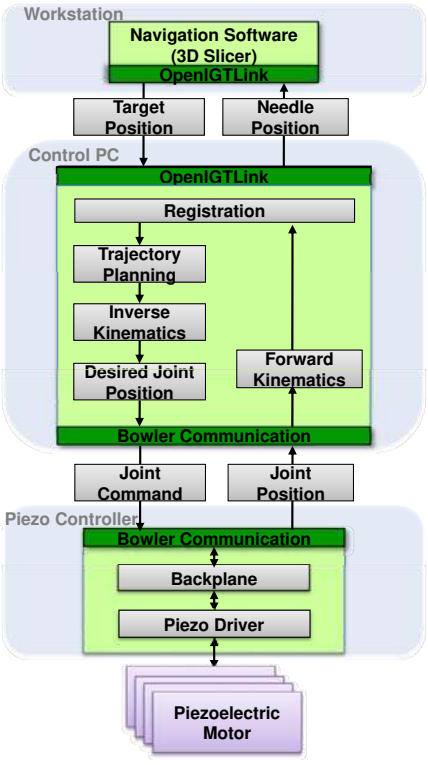

Fig. 2. System architecture for control of the robot.

III. ACTIVE CANNULA KINEMATICS

Our prototype active cannula uses two concentric Nitinol tubes, with an inner Nitinol wire representing a simulated ablator or biopsy needle (these are assigned numbers from largest to smallest, with index 1 indicating the outer tube - see diagram in Fig. 3). The outer tube and inner wire are straight, while the middle tube has a pre-curved section at its tip with a constant curvature k of $0.014mm^{-1}$. Although the innermost element is a flexible wire, for simplicity of exposition we will simply refer to all three of these concentric elements as "tubes".

A. Forward Kinematics

The kinematic equations provided here are similar to those given in [13], with the minor modifications. The robot shape consists of four segments, each with a constant curvature. The curvatures k_2 and k_3 and the length of each of the segments l_1, l_2, l_3, l_4 are calculated from the actuated distances t_1, t_2, t_3, which are the insertion distance of each tube's base from its starting point as measured by the robot's encoders. The starting point (i.e. home position) is defined to be the distances t_1, t_2, t_3 when the tip of each tube is at the Constrained Entry Point. Due to finite clearance between tubes, the middle tube (Tube 2) exits the outer tube (Tube 1) with an angular offset of θ. The lengths of the sections shown in Fig. 3 are given by:

$$l_1 = max(t_2 - L_c, 0),$$

$$l_2 = max(t_1 - l_1, 0),$$

$$l_3 = max(t_2 - l_2 - l_1, 0),$$

$$l_4 = max(t_3 - l_3 - l_2 - l_1 c, 0)$$

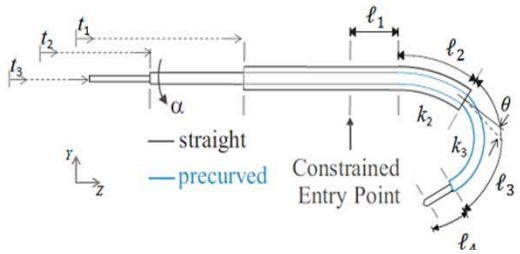

Fig. 3. Illustration of the 3-part concentric tube continuum manipulator shown with the variables used for active cannula kinematics.

The curvatures of the overlapping sections are:

$$k_2 = \frac{E_2 I_2}{E_1 I_1 + E_2 I_2 + E_3 I_3} k,$$

$$k_3 = \frac{E_2 I_2}{E_2 I_2 + E_3 I_3} k$$

where E_i is the Young's Modulus of the i^{th} tube and I_i is the cross sectional moment of inertia of the tube, and L_C is the length of the pre-curved section of the middle tube (Tube 2). Forward kinematics consists of the series of homogenous transformations:

$$T_{tip} = T_\alpha T_1 T_2 T_\theta T_3 T_4$$

where intermediate transformations are defined as:

$$T_\alpha = \begin{bmatrix} cos\alpha & -sin\alpha & 0 & 0 \\ sin\alpha & cos\alpha & 0 & 0 \\ 0 & 0 & 0 & 0 \\ 0 & 0 & 0 & 1 \end{bmatrix}$$

$$T_1 = \begin{bmatrix} 1 & 0 & 0 & 0 \\ 0 & 1 & 0 & 0 \\ 0 & 0 & 0 & l_1 \\ 0 & 0 & 0 & 1 \end{bmatrix}$$

$$T_2 = \begin{bmatrix} 1 & 0 & 0 & 0 \\ 0 & cos(k_2 l_2) & -sin(k_2 l_2) & \frac{cos(k_2 l_2)-1}{k_2} \\ 0 & sin(k_2 l_2) & cos(k_2 l_2) & \frac{sin(k_2 l_2)}{k_2} \\ 0 & 0 & 0 & 1 \end{bmatrix}$$

$$T_\theta = \begin{bmatrix} 1 & 0 & 0 & 0 \\ 0 & cos\theta & -sin\theta & 0 \\ 0 & sin\theta & cos\theta & 0 \\ 0 & 0 & 0 & 1 \end{bmatrix}$$

$$T_3 = \begin{bmatrix} 1 & 0 & 0 & 0 \\ 0 & cos(k_3 l_3) & -sin(k_3 l_3) & \frac{cos(k_3 l_3)-1}{k_{123}} \\ 0 & sin(k_3 l_3) & cos(k_3 l_3) & \frac{sin(k_3 l_3)}{k_3} \\ 0 & 0 & 0 & 1 \end{bmatrix}$$

$$T_4 = \begin{bmatrix} 1 & 0 & 0 & 0 \\ 0 & 1 & 0 & 0 \\ 0 & 0 & 1 & l_4 \\ 0 & 0 & 0 & 1 \end{bmatrix}$$

Thus, T_{tip} gives the position and orientation of the tip of the cannula as a function of the measured actuator configurations: t_1, t_2, t_3, and α.

B. Inverse Kinematics

To place the tip of the active cannula at a desired target, we must invert the forward kinematic mapping given in Section III-A. To do this, we performed a nonlinear optimization using Matlab's *fminsearch* function. This enables us to determine the actuator values which minimize the difference between the kinematic model-predicted and desired tip positions. To provide the algorithm with an initial guess, we first sampled the cannula's configuration space using a uniform discretization of 100 actuator configurations, and computed the tip position at each configuration. We then used the configuration with the lowest tip distance to the desired target as our initial guess.

IV. ROBOTIC SYSTEM DESIGN

A. MR-Compatible Concentric Tube Manipulator

The robotic system is an MRI-compatible piezoelectric actuated robot for precise control of the three concentric tubes forming the active cannula. It was adapted from [27] which was intended for performing prostate biopsy with real-time, in situ guidance in 3T MRI. The 6-DOF robot consists of a modular 3-DOF cannula driver with fiducial tracking frame and a 3-DOF actuated Cartesian stage. The cannula driver provides 2-DOF rotation and translation of the pre-curved middle tube (Tube 2) and 1-DOF translation of the innermost stylet (Tube 3). This compact mechanism utilizes disposable collect fixture and a timing belt mechanism is used to drive the rotation motion. The Cartesian stage provides 2-DOF lateral motion for alignment and 1-DOF for control of the outer cannula (Tube 1) along the insertion axis.The system utilizes piezoelectric actuators (PiezoMotor, Uppsala, Sweden) which are described further in Section IV-B and optical encoders (US Digital, Vancouver, Washington) to provide position sensing feedback for closed-loop control of each axis. Fig. 4 is a detailed view of the active cannula robot.

Resolution of the linear quadrature optical encoders integrated into the robot is 0.0127 mm/count (0.0005" resolution). A digital dial gauge with the same resolution is utilized for independent assessment of the robot's joint space accuracy. Each linear axis of robot (outer, middle and inner tube) is commanded to move in 1 mm increments 40 times and the relative change in dial gauge reading is recorded. The joints can be reliably controlled to within 30μm.

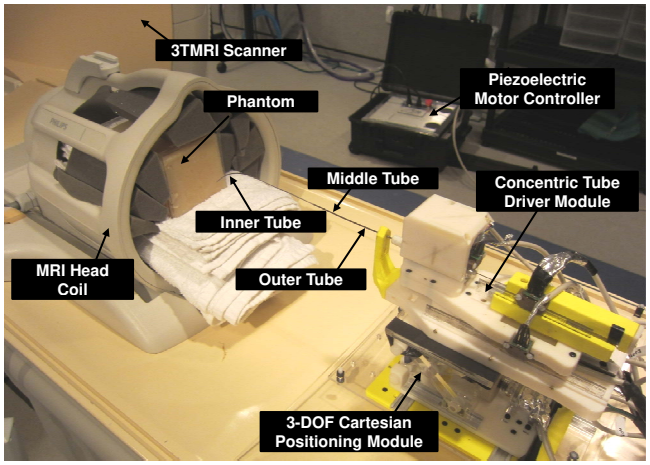

Fig. 4. Active cannula manipulation robot configured for phantom trials inside a 3T MRI scanner and the piezoelectric motor controller is shown inside scanner room. Cannula is shown in an extended configuration.

B. MR-Compatible Piezoelectric Actuation System

We present a generalized piezoelectric actuator driver and control system for use with MRI-guided interventional systems. Fig. 5 shows the robot controller enclosure which houses the custom-made piezoelectric motor driver boards configured for 5-axis control. The driver boards are capable of driving and controlling multiple actuator styles; through only minor software changes, the system supports all commonly used MRI-compatible piezoelectric actuators of both harmonic and non-harmonic types including: Nanomotion (www.nanomotion.com), Piezomotor (www.piezomotor.se), Shinsei (www.shinsei-motor.com), and PCB Motor (www.pcbmotor.com) products. Further, it can be configured to control other actuation systems including pneumatics and hydraulics as well as to perform therapeutic procedures under real-time MRI guidance through powering interstitial ultrasonic ablation probes.

Each non-harmonic piezoelectric motor utilized here uses four distinct waveforms to actuate the piezoelectric elements

inside as shown in as shown Fig. 6 (top). The controller consists of four arbitrary frequency waveform synthesizers, one for each set of elements as shown in Fig. 6 (bottom). Each of the elements is actuated with these four different waveforms at the same time with the same frequency. For this motor type, the drive velocity is proportional to frequency.

Fig. 5. The MRI robot controller (left) is a fully shielded enclosure containing the piezoelectric motor drivers, power supplies, and fiber optic communications in a portable case. The custom-developed piezoelectric motor controller driver boards (right), shown in the 5-axis configuration on a backplane that resides in the shielded enclosure.

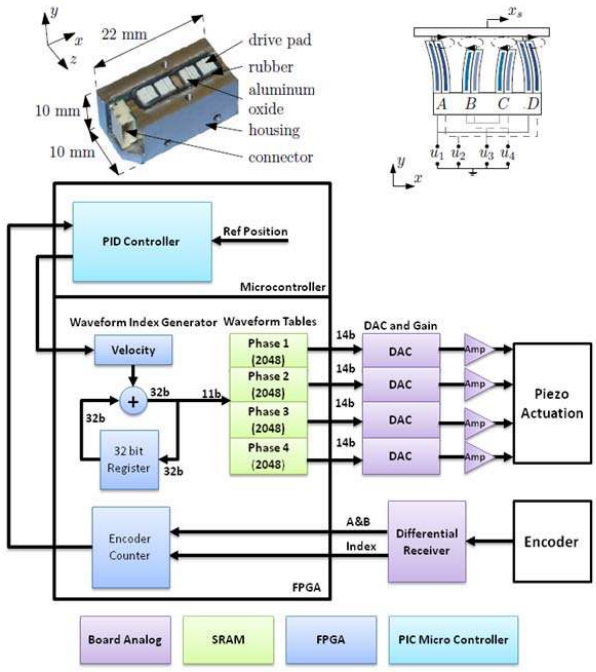

Fig. 6. The piezoelectric actuators utilized in this robot (top-left) have ceramic "fingers" that oscillate based on four specific drive waveforms to generate translational motion (top-right) [28]. A block diagram of the system components of each piezoelectric motor driver board. An FPGA is configured as a waveform synthesizer generate the four phases of the drive signal which are passed to a linear amplifier stage with integrated filtering.

Commercial drivers use a class-D style amplification system that generates the wave forms by low-pass filtering high frequency square waves. While this is efficient, it generates significant high frequency noise that is very difficult to filter or shield without affecting motor operation. Our driver shown in Fig. 6 (bottom) uses four class AB linear amplifiers which generate significantly cleaner drive signals.

As shown in the Fig. 6 (bottom), the controller receives an input in the form of a velocity or position set point. In order to achieve closed-loop position and velocity control, differential encoder signals are interpreted by the FPGA that are fed into an onboard microcontroller that incorporated a joint-level controller that controls the output sample rate of the FPGA's waveform synthesizer. The waveform synthesizer running on the FPGA is used to generate four independent motor-specific control waveforms of arbitrary phase and frequency. These control waveforms are then streamed out to the analog amplification stage at 25 mega samples per second. The driver boards include a high power output amplification stage, which passes the signals from four linear amplifiers out to the actuators through π filters to further remove high frequency noise.

The generalized piezoelectric driving system was created to be a development platform for the control and operation of MRI compatible piezoelectric actuation devices. As such, it was determined that this equipment should be both robust, physically durable, and portable such that it can be moved to and from a laboratory environment to a hospital environment as well as being capable of transported long distances. To this end, the electronics system has been fitted with a shock absorption system, and has been mounted in a modular Faraday cage to shield electrical noise and fitted with tool free fasteners such that it can easily be maintained in the field. In addition, the driver board, backplane, onboard power regulation, and controller enclosure are grounded, shielded and filtered specifically for operation in the MRI environment. This is then mounted in a plastic rugged, wheeled travel case selected to be within the size restrictions for carry-on luggage to allow the system to be easily and safely deployed at multiple locations.

MRI compatibility of the robotic system with the piezoelectric actuator driver was assessed in a similar configuration to [29] inside a 3 Tesla MRI scanner (Philips Achieva). Four imaging protocols were selected for evaluation of compatibility of the system: 1) diagnostic imaging T1-weighted fast gradient echo (T1 FGE/FFE), 2) diagnostic imaging T2-weighted fast spin echo (T2 FSE/TSE), 3) high speed real-time imaging fast gradient echo (FGRE), and 4) functional imaging spin echo-planar imaging (SE EPI). The images were acquired in three states: baseline with no robot or controller, robot and controller present but off, and robot moving inside the imaging volume. As described further in [27], no statistically significant image quality degradation - defined as signal-to-noise ratio loss - is evident during simultaneous robot motion and imaging.

C. Multi-Slice Based Fiducial Registration

The robot is registered to the patient coordinate system - referred to as right-anterior-supine (RAS) coordinates - based on imaging a fiducial frame attached to the robot as shown in Fig. 7. The fiducial frame is made of seven tubes filled with high contrast fluid and configured in a set of Z shapes in three orthogonal planes [3]. In prior work we have performed 6-DOF registration using a single image slice which provides convenience and speed at the expense of accuracy [3] [30]. A new approach [31] is utilized wherein multiple slices of the frame are used together to determine the 6-DOF position

and orientation of the frame on the robot with respect to the scanner.

Fig. 7 (bottom) illustrates one T2-weighted fast spin echo image of tracking fiducial frame. The registration algorithm first segments the image and compensates for the irregular shape of the fiducial to find the best fitting ellipse as shown. The seven points from several slices are then utilized to calculate the 6-DOF position and orientation of the robot with respect to the scanner origin. An independent evaluation of registration accuracy in the MRI scanner showed sub-pixel resolution with a mean error of 0.27 mm in translation and 0.16° in orientation; the corresponding RMS error is 0.33mm and 0.46° in terms of ground truth obtained from calibrated benchtop position and orientation model [31].

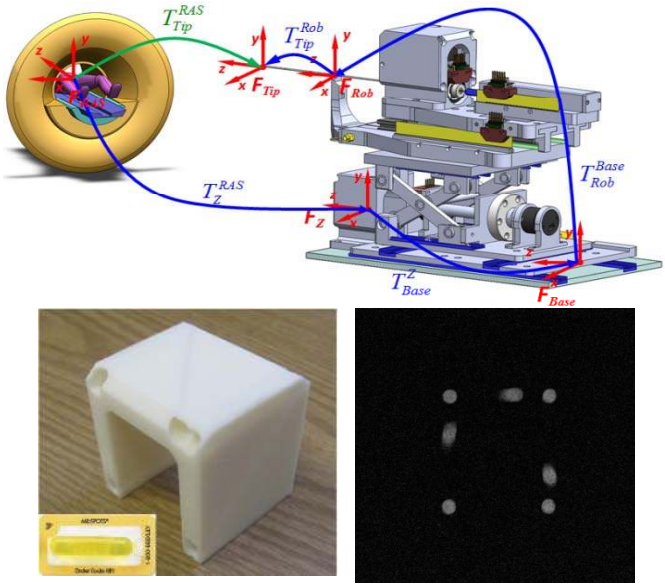

Fig. 7. Coordinate frames of the robotic system for registration of the robot to MR image space (i.e. patient coordinates) and determining the active required cannula kinematics (Top). The Z-frame registration fiducial with corresponding cross-sectional MR image (Bottom).

The corresponding series of homogeneous transformations is used to determine the continuum robot's tip location in MR image coordinates (i.e. RAS coordinates):

$$T_{Tip}^{RAS} = T_{Z}^{RAS} \cdot T_{Base}^{Z} \cdot T_{Rob}^{Base} \cdot T_{Tip}^{Rob}$$

where T_{Tip}^{RAS} is the needle tip in the RAS patient coordinate system, T_{Z}^{RAS} is the fiducial's 6-DOF coordinates in RAS coordinates as determined by the Z-frame fiducial-based registration, T_{Base}^{Z} is the mechanically fixed location of the fiducial on the robot, T_{Rob}^{Base} is the robot end effector location with respect to the robot base as determined from the forward kinematics of the base robot, and T_{Tip}^{Rob} is the needle tip with respect to the end effector of the robot as determined by the active cannula kinematics defined in Section III.

In the navigation software, a desired T_{Tip}^{RAS} is selected from the MR image volume. This desired position T_{Tip}^{RAS} is sent to the robot control interface software from the planning workstation to use inverse kinematics to calculate the required joint positions, which are transmitted to the robot controller to drive piezoelectric actuators.

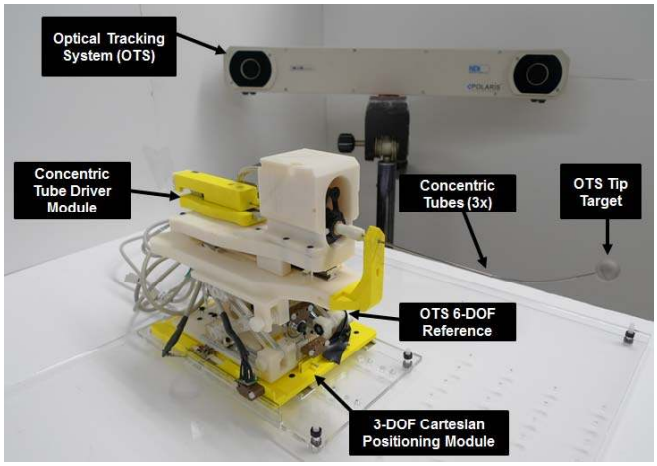

Fig. 8. Piezoelectrically actuated concentric tube robot shown in the configuration for benchtop accuracy assessment trials.

V. EXPERIMENTS AND RESULTS

A. Continuum Robot Accuracy Assessment Utilizing Optical Tracking

The robot task space accuracy is evaluated by a Polaris (Northern Digital, Ontario, Canada) optical tracking system (OTS). The stated 3D volumetric accuracy of the Polaris is 0.35 mm, and based on our assessment the standard deviation of readings for a given stable point is 0.10 mm. A 6-DOF reference frame consisting of a circular plate and three passive spheres is rigidly mounted to the base of the robot and another passive sphere is mounted at the tip of the active cannula as shown in Fig. 9.

The robot tip position is measured in each configuration by collecting 300 readings at 30 Hz. The robot base frame was registered to OTS via a point based registration [13] based on a set of 12 known points in each coordinate system (OTS & robot). This registration identifies the frame transformation of the 6-DOF reference frame with respect to the robot base frame. The active cannula is moved to seven orientations in each of three depths (middle tube translation = 30 mm, 40 mm and 50 mm). In each of the 21 configurations, the forward kinematics of the cannula is calculated based on the corresponding robot configuration. The theoretical tip position is then compared to the tip location resolved by the OTS (after being transformed in the robot's coordinate system).

The results from the benchtop evaluation are shown in Fig. 9. The actual tip locations (as measured by the OTS) are shown with blue stars, and the theoretical tip position calculated based on the registration and continuum robot kinematics is shown with red circles. Qualitatively, it is clear that the active cannula spirals around three planes and tracks the theoretical model location. The RMS error in tip placement in the benchtop trials using an external optical tracking system is 1.00 mm.

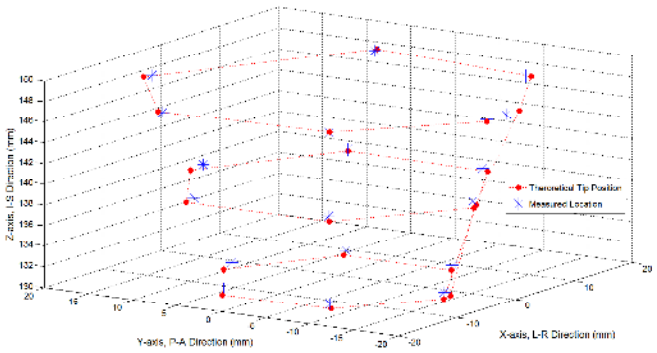

Fig. 9. Benchtop evaluation of the accuracy of the active cannula robot. Actual tip locations as the active cannula was moved to 7 points in each of three planes as measured by the optical tracker (blue stars) and the calculated theoretical tip position based on the registration and continuum robot kinematics (red circles).

	Modeled Location	MRI Data	Tip Error
Red	-8.35 35.18 -26.49	-7.14 35.23 -26.48	1.21mm
Yellow	4.06 23.61 -26.25	3.52 23.37 -26.40	0.61mm
Green	-8.14 23.20 -26.49	-7.36 23.41 -24.40	2.24mm

TABLE I

ACTUAL AND THEORETICAL TIP POSITIONS

B. Accuracy Assessment in MRI Phantom Trials

The robot was furthered evaluated by active cannula steering under MR imaging. The phantom tissue used for the experiments was simulated muscle ballistic test media (Corbin, Inc., USA). The rubber-like material was molded into a $10cm \times 10cm \times 10cm$ rectangular form. This phantom was placed inside a head coil, and the robot was initialized to home position in front of the phantom as shown in Fig. 4.

A diagnostic imaging T2-weighted fast spin echo protocol (repetition time 2700 ms, echo time 22 ms, slice thickness 2 mm, $0.5mm \times 0.5mm$ pixel size) is utilized to visualize the needle insertion trajectory. 44 image slices of the phantom are acquired inside a 3 Tesla Philips Achieva scanner. Three trajectories were evaluated in the phantom in the MRI as shown in Fig. 10.

The following procedure ensures that the active cannula follows the desired trajectory (i.e. the shaft follows the tip exactly) as it is inserted into the phantom: the motion begins with all three tubes such that their tips are at the entry point and the rotation of the middle tube set to the desired angle, then all three tubes move forward together a distance $l_1 + l_2$, then the outer tube is stopped and the inner two tubes translate simultaneously a distance l_3, and finally the middle tube is stopped and the innermost tube is extended a distance l_4. In this experiment, the three trajectories correspond to a translation of the middle tube (Tube 2) of 45 mm at rotation angles of $0°$, $90°$, and $180°$. Fig. 1 shows the MR image volume for one of the curved trajectories. In this image, the

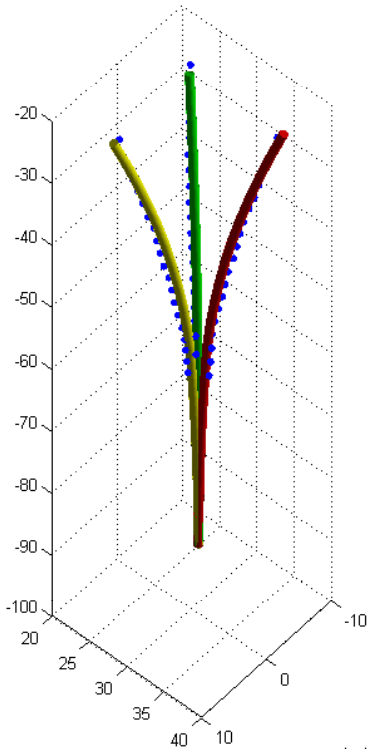

Fig. 10. Results from three robotic active cannula insertion trials inside the MRI scanner. Blue dots represent the measured tip position from the acquired MR image volume. Red, Green, and Yellow tubes represent the theoretical trajectory based on the kinematic model.

44 axial slices ($0.5mm \times 0.5mm \times 2.0mm$ voxel size) are compounded into a 3D volume which is re-sliced into the three orthogonal planes shown. In each set of MR images, the 3D trajectory of the inserted cannula is measured by determining the location of the corresponding signal void in each slice. Fig. 10 shows results from the three robotic active cannula insertion trials overlaid with the theoretical model. Blue dots represent the measured tip position from the acquired MR image volume. The three cylindrical tubes represent the theoretical trajectory based on the kinematic model. The theoretical tip position calculated from the model and the segmented position from the MRI needle void are shown in Table I. The Cartesian positioning errors of the three trajectories are: 1.21 mm, 0.61 mm, and 2.24 mm.

VI. CONCLUSION

This paper presents an MR image-guided concentric tube continuum robotic system with piezoelectric actuation. The robot provides motion with joint-level precision of better than 0.03 mm, and is fully MRI-compatible allowing simultaneous cannula motion and imaging with no image quality degradation. The MRI compatibility, joint space accuracy, task space accuracy and MRI-guided needle placement were evaluated to validate the system's targeting ability in image-guided surgery. RMS error in free space of active cannula placement was 1.00 mm and three trajectories executed inside MRI showed an accuracy of 0.61 - 2.24 mm. The

errors present are due to sensor error (MRI needle artifact and imaging resolution or OTS accuracy), manipulator positioning error, calibration error, and unmodeled frictional forces and tissue interaction forces on the active cannula. These errors will, for the most part, be fully addressed through the use of fully image-guided closed-loop control.

VII. Acknowledgements

This work is supported in part by the Congressionally Directed Medical Research Programs Prostate Cancer Research Program New Investigator Award W81XWH-09-1-0191 and NSF CAREER Award IIS-1054331.

References

[1] Z. Neubach and M. Shoham, "Ultrasound-guided robot for flexible needle steering," *Biomedical Engineering, IEEE Transactions on*, vol. 57, pp. 799 –805, april 2010.

[2] C. J. Walsh, N. C. Hanumara, A. H. Slocum, J.-A. Shepard, and R. Gupta, "A patient-mounted, telerobotic tool for ct-guided percutaneous interventions," *Journal of Medical Devices*, vol. 2, no. 1, pp. 011007–10, 2008.

[3] G. S. Fischer, I. I. Iordachita, C. Csoma, J. Tokuda, S. P. DiMaio, C. M. Tempany, N. Hata, and G. Fichtinger, "MRI-Compatible Pneumatic Robot for Transperineal Prostate Needle Placement," *IEEE/ASME Transactions on Mechatronics*, vol. 13, no. 3, 2008.

[4] A. Krieger, S. Song, N. Bongjoon Cho, I. I. Iordachita, P. Guion, G. Fichtinger, and L. L. Whitcomb, "Development and Evaluation of an Actuated MRI-Compatible Robotic System for MRI-Guided Prostate Intervention," *Mechatronics, IEEE/ASME Transactions on*, vol. PP, no. 99, pp. 1–12, 2011.

[5] J. A. Cunha, I.-C. Hsu, J. Pouliot, M. Roach III, K. Shinohara, J. Kurhanewicz, G. Reed, and D. Stoianovici, "Toward adaptive stereotactic robotic brachytherapy for prostate cancer: Demonstration of an adaptive workflow incorporating inverse planning and an mr stealth robot," *Minimally Invasive Therapy and Allied Technologies*, vol. 19, no. 4, pp. 189–202, 2010.

[6] S. DiMaio and S. Salcudean, "Needle insertion modeling and simulation," *Robotics and Automation, IEEE Transactions on*, vol. 19, pp. 864 – 875, oct. 2003.

[7] D. Glozman and M. Shoham, "Image-guided robotic flexible needle steering," *Robotics, IEEE Transactions on*, vol. 23, pp. 459 –467, jun. 2007.

[8] R. J. Webster III, J. S. Kim, N. Cowan, G. Chirikjian, and A. Okamura, "Nonholonomic modeling of needle steering," *International Journal of Robotics Research*, vol. 25, no. 5-6, pp. 509–25, 2006.

[9] P. Dupont, J. Lock, B. Itkowitz, and E. Butler, "Design and control of concentric-tube robots," *Robotics, IEEE Transactions on*, vol. 26, pp. 209 –225, april 2010.

[10] D. Rucker, B. Jones, and R. J. Webster III, "A geometrically exact model for externally loaded concentric-tube continuum robots," *Robotics, IEEE Transactions on*, vol. 26, pp. 769 –780, oct. 2010.

[11] J. Burgner, P. J. Swaney, D. C. Rucker, H. B. Gilbert, S. T. Nill, P. T. Russell, K. D. Weaver, and R. J. Webster III, "A bimanual teleoperated system for endonasal skull base surgery," in *Intelligent Robots and Systems (IROS), 2011 IEEE/RSJ International Conference on*, pp. 2517 –2523, 2011.

[12] E. C. Burdette, D. C. Rucker, P. Prakash, C. J. Diederich, J. M. Croom, C. Clarke, P. Stolka, T. Juang, E. M. Boctor, and I. Webster III, R. J., "The acusitt ultrasonic ablator: the first steerable needle with an integrated interventional tool," *Proceedings of SPIE Medical Imaging*, no. 7629, 2010.

[13] R. Lathrop, D. Rucker, and R. J. Webster III, "Guidance of a steerable cannula robot in soft tissue using preoperative imaging and conoscopic surface contour sensing," in *Robotics and Automation (ICRA), 2010 IEEE International Conference on*, pp. 5601 –5606, may 2010.

[14] G. R. Sutherland, I. Latour, A. D. Greer, T. Fielding, G. Feil, and P. Newhook, "An image-guided magnetic resonance-compatible surgical robot.," *Neurosurgery*, vol. 62, pp. 286–92; discussion 292–3, Feb 2008.

[15] D. Yakar, M. G. Schouten, D. G. H. Bosboom, J. O. Barentsz, T. W. J. Scheenen, and J. J. Ftterer, "Feasibility of a pneumatically actuated mr-compatible robot for transrectal prostate biopsy guidance," *Radiology*, vol. 260, no. 1, pp. 241–247, 2011.

[16] B. Yang, U. Tan, R. Gullapalli, A. McMillan, and J. Desai, "Design and Implementation of a Pneumatically-Actuated Robot for Breast Biopsy under Continuous MRI," IEEE ICRA 2011 International Conference on Robotics and Automation, (Shanghai, China), 2011.

[17] S.-E. Song, N. Cho, G. S. Fischer, N. Hata, C. Tempany, G. Fichtinger, and I. Iordachita, "Development of a pneumatic robot for MRI-guided transperineal prostate biopsy and brachytherapy: New approaches," in *Robotics and Automation (ICRA), 2010 IEEE International Conference on*, pp. 2580 –2585, may 2010.

[18] R. Seifabadi, S.-E. Song, A. Krieger, N. B. Cho, J. Tokuda, G. Fichtinger, and I. Iordachita, "Robotic System for MRI-guided Prostate Biopsy: Feasibility of Teleoperated Needle Insertion and ex vivo Phantom Study," *International Journal of Computer Aided Radiology and Surgery (IJCARS)*, 2011.

[19] K. Chinzei, N. Hata, F. A. Jolesz, and R. Kikinis, "MRI Compatible Surgical Assist Robot: System Integration and Preliminary Feasibility Study," in *MICCAI*, vol. 1935, pp. 921–930, October 2000.

[20] H. Elhawary, Z. Tse, M. Rea, A. Zivanovic, B. Davies, C. Besant, N. de Souza, D. McRobbie, I. Young, and M. Lamperth, "Robotic System for Transrectal Biopsy of the Prostate: Real-Time Guidance Under MRI," *Engineering in Medicine and Biology Magazine, IEEE*, vol. 29, pp. 78 –86, march-april 2010.

[21] G. S. Fischer, A. Krieger, I. I. Iordachita, C. Csoma, L. L. Whitcomb, and G. Fichtinger, "MRI Compatibility of Robot Actuation Techniques – A Comparative Study," *Int Conf Med Image Comput Comput Assist Interv*, Sept. 2008.

[22] G. S. Fischer, G. Cole, and H. Su, "Approaches to creating and controlling motion in MRI," in *Engineering in Medicine and Biology Society,EMBC, 2011 Annual International Conference of the IEEE*, pp. 6687–6690, 2011.

[23] H. Su, G. A. Cole, C. Tempany, N. Hata, and G. S. Fischer, "High-Field MRI-Compatible Needle Placement Robot for Prostate Interventions," in *MMVR18 (Medicine Meets Virtual Reality)*, 2011.

[24] H. Su, G. A. Cole, and G. S. Fischer, "High-field MRI-Compatible needle placement robots for prostate interventions: pneumatic and piezoelectric approaches," *Robotics and Virtual Reality (T. Gulrez and A. Hassanien, eds.)*, 2011.

[25] G. Cole, K. Harrington, H. Su, A. Camilo, J. Pilitsis, and G. Fischer, "Closed-Loop Actuated Surgical System Utilizing Real-Time In-Situ MRI Guidance," 12th International Symposium on Experimental Robotics - ISER 2010, (New Delhi and Agra, India), Dec 2010.

[26] J. Tokuda, G. S. Fischer, X. Papademetris, Z. Yaniv, L. Ibanez, P. Cheng, H. Liu, J. Blevins, J. Arata, A. J. Golby, T. Kapur, S. Pieper, E. C. Burdette, G. Fichtinger, C. M. Tempany, and N. Hata, "Openigtlink: an open network protocol for image-guided therapy environment," *The International Journal of Medical Robotics and Computer Assisted Surgery*, vol. 5, no. 4, pp. 423–434, 2009.

[27] H. Su, M. Zervas, G. Cole, C. Furlong, and G. S. Fischer, "Real-time MRI-Guided Needle Placement Robot with Integrated Fiber Optic Force Sensing," IEEE ICRA 2011 International Conference on Robotics and Automation, (Shanghai, China), 2011.

[28] R. Merry, M. Maassen, M. van de Molengraft, N. van de Wouw, and M. Steinbuch, "Modeling and waveform optimization of a nanomotion piezo stage," *Mechatronics, IEEE/ASME Transactions on*, vol. 16, no. 4, pp. 615–626, 2011.

[29] H. Su, W. Shang, K. Harrington, A. Camilo, G. A. Cole, J. Tokuda, C. Tempany, N. Hata, and G. S. Fischer, "A Networked Modular Hardware and Software system for MRI-guided Robotic Prostate Interventions," in *SPIE Medical Imaging (Image-Guided Procedures, Robotic Interventions, and Modeling Conference)*, (San Diego, USA), 2012.

[30] J. Tokuda, G. S. Fischer, S. P. DiMaio, D. G. Gobbi, C. Csoma, P. W. Mewes, G. Fichtinger, C. M. Tempany, and N. Hata, "Integrated navigation and control software system for MRI-guided robotic prostate interventions," *Computerized Medical Imaging and Graphics*, vol. 34, no. 1, pp. 3 – 8, 2010.

[31] W. Shang and G. S. Fischer, "A High Accuracy Multi-Image Registration Method for Tracking MRI-Guided Robots," in *SPIE Medical Imaging (Image-Guided Procedures, Robotic Interventions, and Modeling Conference)*, (San Diego, USA), 2012.